NANO LETTERS

Letter

pubs.acs.org/NanoLett

Current-Phase Relation of Ballistic Graphene Josephson Junctions

G. Nanda,[†] J. L. Aguilera-Servin,[†,∞] P. Rakyta,[¶] A. Kormányos,[§] R. Kleiner,[‖] D. Koelle,[‖] K. Watanabe,[⊥] T. Taniguchi,[⊥] L. M. K. Vandersypen,[†,#] and S. Goswami*[,†,#]

[†]Kavli Institute of Nanoscience, Delft University of Technology, 2600 GA Delft, The Netherlands

[∞]Institute of Science and Technology Austria, Am Campus 1, A-3400 Klosterneuburg, Austria

[¶]Department of Physics of Complex Systems, Eötvös University, Pázmány Péter Sétány 1/A, H-1117 Budapest, Hungary

[§]Department of Physics, University of Konstanz, D-78464 Konstanz, Germany

[‖]Physikalisches Institut and Center for Quantum Science (CQ) in LISA+, Eberhard Karls Universität Tübingen, Auf der Morgenstelle 14, D-72076 Tübingen, Germany

[⊥]National Institute for Materials Science, 1-1 Namiki, Tsukuba, 305-0044, Japan

[#]QuTech, Delft University of Technology, 2600 GA Delft, The Netherlands

Supporting Information

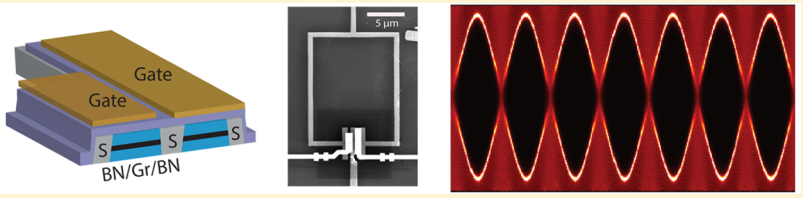

ABSTRACT: The current-phase relation (CPR) of a Josephson junction (JJ) determines how the supercurrent evolves with the superconducting phase difference across the junction. Knowledge of the CPR is essential in order to understand the response of a JJ to various external parameters. Despite the rising interest in ultraclean encapsulated graphene JJs, the CPR of such junctions remains unknown. Here, we use a fully gate-tunable graphene superconducting quantum intereference device (SQUID) to determine the CPR of ballistic graphene JJs. Each of the two JJs in the SQUID is made with graphene encapsulated in hexagonal boron nitride. By independently controlling the critical current of the JJs, we can operate the SQUID either in a symmetric or asymmetric configuration. The highly asymmetric SQUID allows us to phase-bias one of the JJs and thereby directly obtain its CPR. The CPR is found to be skewed, deviating significantly from a sinusoidal form. The skewness can be tuned with the gate voltage and oscillates in antiphase with Fabry-Pérot resistance oscillations of the ballistic graphene cavity. We compare our experiments with tight-binding calculations that include realistic graphene−superconductor interfaces and find a good qualitative agreement.

KEYWORDS: *Graphene, Josephson junctions, SQUID, current-phase relation*

The past few years have seen remarkable progress in the study of graphene-superconductor hybrids. This surge in interest has primarily been driven by the ability to combine high-quality graphene with superconductors via clean interfaces and has led to several experimental advances. These include the observation of specular Andreev reflection,[1] crossed Andreev reflections,[2] and superconducting proximity effects in ballistic graphene Josephson junctions (JJs).[3−7] In a majority of these studies the device comprises of graphene encapsulated in hexagonal boron nitride (BN) contacted along the edge by a superconductor. The encapsulation in BN keeps the graphene clean, while the edge contacting scheme provides transparent interfaces. In particular, ballistic JJs fabricated in this manner have been central to recent studies of novel Andreev bound states in perpendicular magnetic fields,[4] edge-mode superconductivity,[5] and supercurrents in the quantum Hall regime.[6] However, to date there have been no measurements of the Josephson current phase relation (CPR) in these systems.

The CPR is arguably one of the most basic properties of a JJ and provides information about the Andreev bound state (ABS) spectrum in the junction. While typical superconductor−insulator−superconductor (SIS) JJs exhibit a sinusoidal CPR, deviations from this behavior can be present in superconductor−normal−superconductor (SNS) junctions. Examples of this include JJs with high transmission such as nanowires[8,9] and atomic point contacts,[10,11] where the CPR contains significant higher frequency components. Furthermore, the periodicity of the CPR itself can be different from 2π for more exotic systems such as topological JJs.[12] For graphene JJs, there have been several numerical estimates of the CPR which take into account its linear dispersion relation.[13−17] More recently, ballistic graphene JJs operated in large magnetic fields

Received: January 9, 2017
Revised: May 3, 2017
Published: May 5, 2017

DOI: 10.1021/acs.nanolett.7b00097
Nano Lett. XXXX, XXX, XXX−XXX

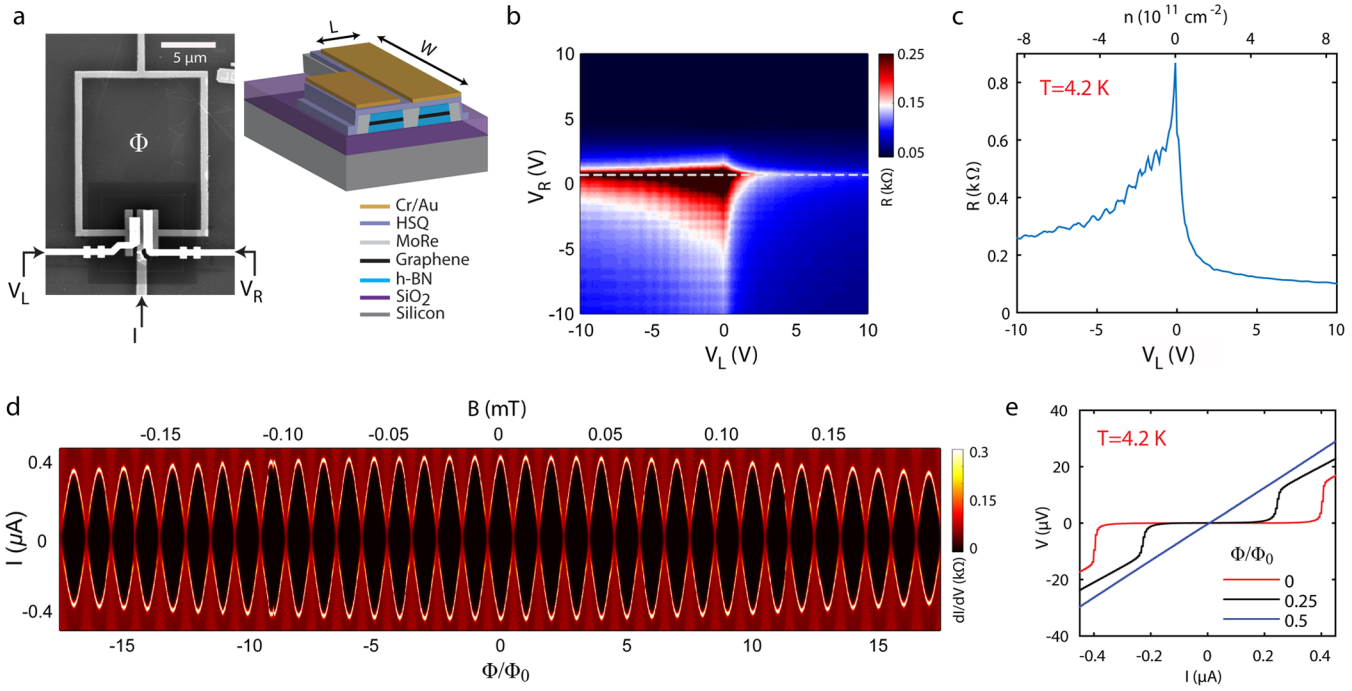

Figure 1. (a) Scanning electron micrograph of the graphene dc-SQUID (Dev1) along with a cross-sectional schematic. Gate voltages V_L and V_R independently control the carrier density of the left and right junction, respectively. (b) Resistance R across the SQUID versus V_L and V_R, demonstrating independent control of carrier type and density in the JJs. The bias current (I) for these measurements was fixed at 500 nA. (c) Line trace taken along the dashed white line in (b) showing Fabry-Pérot oscillations in the hole-doped regime. (d) Differential resistance dV/dI as a function of dc current bias I and magnetic field B with the SQUID operated in a symmetric configuration (V_L = +10 V and V_R = +2.5 V). Flux-periodic oscillations are clearly visible with a slowly decaying envelope arising from the interference pattern of a single JJ. (e) V−I plots [extracted from (d)] for different values of magnetic flux Φ showing a nearly 100% modulation of the critical current. All measurements shown here are performed at T = 4.2 K.

have been predicted to undergo a topological transition,[18] which should be detectable via direct CPR measurements. However, the experimental determination of the CPR in graphene has been restricted to junctions that are either in the diffusive limit[19] or in a geometry that does not allow gate control of the junction properties.[20]

Here, we use a direct current (dc) superconducting quantum interference device (SQUID) to directly determine the CPR in encapsulated graphene JJs. These graphene SQUIDs stand out from previous studies[21,22] in two important ways. First, the superconducting contacts are made with molybdenum rhenium (MoRe), which allows us to operate the SQUID up to 4.2 K. More importantly, our SQUID consists of graphene JJs that are ballistic and independently tunable, thereby allowing full electrostatic control over the SQUID response. By applying appropriate gate voltages we can continuously tune from a symmetric to an asymmetric SQUID. We show that the asymmetric configuration allows us to directly extract the CPR from flux periodic oscillations in the critical current of the SQUID. The CPR is found to be nonsinusoidal, displaying a prominent forward skewing. This skewness can be tuned over a large range with the gate voltage and shows correlations with Fabry-Pérot (FP) resistance oscillations in the ballistic cavity. We complement our experiments with tight-binding simulations that go beyond the short junction limit and explicitly take into account realistic graphene−superconductor interfaces.

Figure 1a shows a scanning electron micrograph and cross-sectional schematic of a device. It consists of two encapsulated graphene JJs contacted with MoRe, incorporated in a SQUID loop. The fabrication strategy is similar to earlier work[3] and further details are provided in the Supporting Information (SI). The left (L-JJ)/right (R-JJ) JJs can be tuned independently by applying voltages (V_L/V_R) to local top gates. The junctions are intentionally designed to have a geometrical asymmetry, which ensures that the critical current of R-JJ (I_{cR}) is larger than that of L-JJ (I_{cL}) at the same carrier density. We report on two devices (Dev1 and Dev2) both of which have the same lithographic dimensions ($L \times W$) for L-JJ (400 nm × 2 μm). The dimensions of R-JJ for Dev1 and Dev2 are 400 nm × 4 μm and 400 nm × 8 μm, respectively. All measurements were performed using a dc current bias applied across the SQUID in a dilution refrigerator with a base temperature of 40 mK.

Figure 1b shows the variation in the normal state resistance (R) of the SQUID with V_L and V_R at T = 4.2 K. The device was biased with a relatively large current of 500 nA, which is larger than the critical current of the SQUID for most of the gate range. Figure 1c shows a single trace taken along the white dashed line of Figure 1b, where R-JJ is held at the charge neutrality point (CNP). We see clear FP oscillations on the hole (p) doped region due to the formation of n−p junctions at the superconductor−graphene interfaces.[3,4] Furthermore, the criss-cross pattern seen in the lower left quadrant of Figure 1b indicates that both graphene junctions are in the ballistic limit and that there is no cross-talk between the individual gates. We note that when V_R > 3 V the critical current of the SQUID (I_c) is larger than the applied current bias, and a zero-resistance state is thus visible even at 4.2 K. Having established the fact that our JJs are in the ballistic regime, we now look in more detail at the behavior of the SQUID. At T = 4.2 K, we first tune the gate voltages (V_L = +10 V, V_R = +2.5 V) such that the

DOI: 10.1021/acs.nanolett.7b00097
Nano Lett. XXXX, XXX, XXX−XXX

SQUID is in a symmetric configuration and $I_{cR} = I_{cL}$. Figure 1d shows the variation in differential resistance dV/dI with current bias I and magnetic field B, where we observe clear oscillations in I_c with magnetic flux. In this configuration, the modulation in I_c is nearly 100%, as seen by the individual $V-I$ traces in Figure 1e. The slow decay in the maximum value of I_c arises due to the (Fraunhofer) magnetic field response of a single junction. The devices were designed such that this background was negligible around $B = 0$ (that is, the SQUID loop area was kept much larger than the JJ area). Minimizing this background is important for a reliable determination of the CPR, as we will see below.

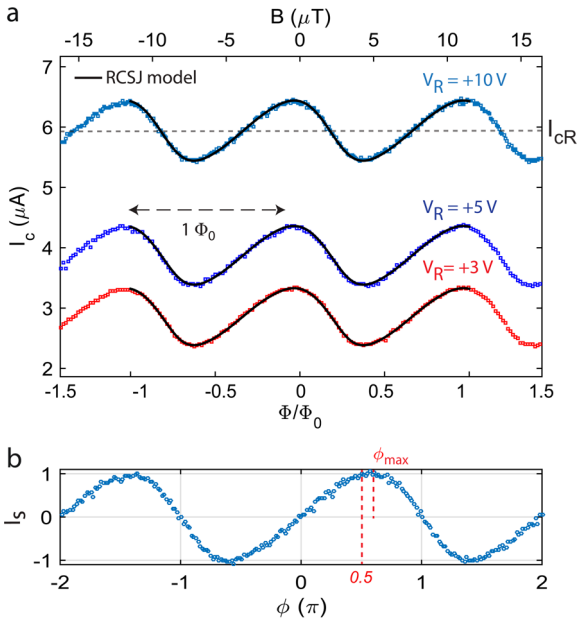

Figure 2. (a) Variation of I_c with Φ for $V_L = -4$ V and $V_R = +10$, +5, and +3 V at 40 mK. Solid black lines are results from RCSJ simulations of the SQUID. (b) Variation of supercurrent $I_s = (I_c - I_{cR})/I_{cL}$ with phase ϕ extracted from the top curve in (a). ϕ_{max} indicates the phase at which I_s reaches a maximum and is noticeably different from $\pi/2$, indicating a forward skewed CPR.

We now turn our attention to the flux-dependent response of a highly asymmetric SQUID ($I_{cR} \gg I_{cL}$), a condition that can be readily achieved by tuning the gate voltages appropriately. To outline the working principle of the device, we start with the assumption that both JJs have a sinusoidal CPR (a more general treatment can be found in the SI). So, the critical current of the SQUID can be written as $I_c = I_{cL} \sin\theta + I_{cR} \sin\delta$, where θ (δ) is the phase drop across L-JJ (R-JJ). When an external magnetic flux (Φ) threads through the SQUID loop, the flux and phase are related by $\delta - \theta = 2\pi\Phi/\Phi_0$, assuming the loop inductance is negligible. Now, when $I_{cR} \gg I_{cL}$ the phase difference across R-JJ is very close to $\pi/2$. Thus, $I_c(\Phi) \approx I_{cR} + I_{cL} \sin(2\pi\Phi/\Phi_0 + \pi/2)$ and the flux-dependence of I_c directly represents the CPR of L-JJ, that is, $I_c(\Phi) \approx I_{cR} + I_s(\phi)$, where I_s is the supercurrent through L-JJ and ϕ is the phase drop across it. This principle of using an asymmetric SQUID to probe the CPR has been employed in the past for systems such as point contacts[10,11] and vertical graphene JJs,[20] where an SIS junction (with a well-known sinusoidal CPR) was used as the reference junction. In our case, the reference junction is also a graphene JJ, where the CPR is not known a priori. We show (see SI) that this does not affect our ability to probe the CPR, provided time reversal symmetry is not broken, meaning that the CPR satisfies the condition $I_s(\phi) = -I_s(-\phi)$.[23] Throughout the remainder of the text we use R-JJ as the reference junction (larger critical current), and L-JJ is the junction under study (smaller critical current).

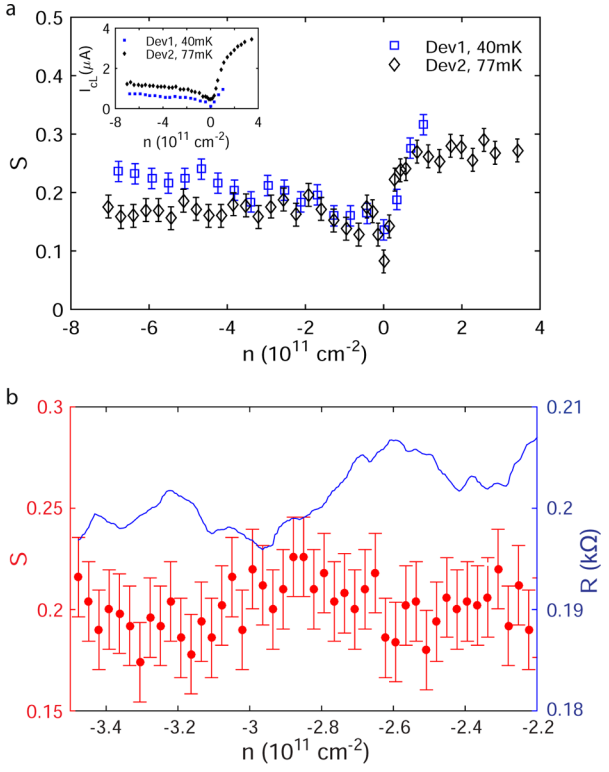

Figure 3. (a) Variation of skewness S as a function of carrier density n for Dev1 and Dev2. The larger geometric asymmetry of Dev2 (see text) allows one to reliably probe the CPR up to higher n-doping. Inset shows the variation of I_{cL} with density. (b) A finer scan for Dev2 shows that S oscillates with carrier density in the p-doped regime in antiphase with Fabry–Pérot oscillations in the resistance.

Figure 2a shows the typical magnetic response of the asymmetric SQUID at $T = 40$ mK with $V_L = -4$ V (fixed) and different values of V_R. For the most asymmetric configuration ($V_R = +10$ V) I_c oscillates around a fixed value of roughly 6 μA (I_{cR}) with an amplitude of about 500 nA (I_{cL}). Using the arguments described above, this $I_c(\Phi)$ curve can be converted to $I_s(\phi)$, as shown in Figure 2b. Here I_s is the normalized supercurrent defined as $(I_c - I_{cR})/I_{cL}$. We note that there is an uncertainty (less than one period) in the exact position of zero B. This, combined with the unknown CPR of the reference graphene JJ, makes it important to do this conversion carefully, and we describe the details in the SI. The CPR shows a clear deviation from a sinusoidal form, showing a prominent forward skewing (that is, I_s peaks at $\phi > \pi/2$). We define the skewness of the CPR as $S = (2\phi_{max}/\pi) - 1$,[19] where ϕ_{max} is the phase for which the supercurrent is maximum.

To be certain that we are indeed measuring the CPR of L-JJ, we perform some important checks. We keep I_{cL} fixed and reduce I_{cR} (by reducing V_R). Figure 2a shows that reducing I_{cR} merely shifts the $I_c(\Phi)$ downward and therefore does not affect the extracted CPR, as one would expect. Furthermore, we use the experimentally determined CPR (from Figure 2b), the junction asymmetry, and loop inductance as inputs for the resistively and capacitively shunted junction (RCSJ) model to

DOI: 10.1021/acs.nanolett.7b00097
Nano Lett. XXXX, XXX, XXX−XXX

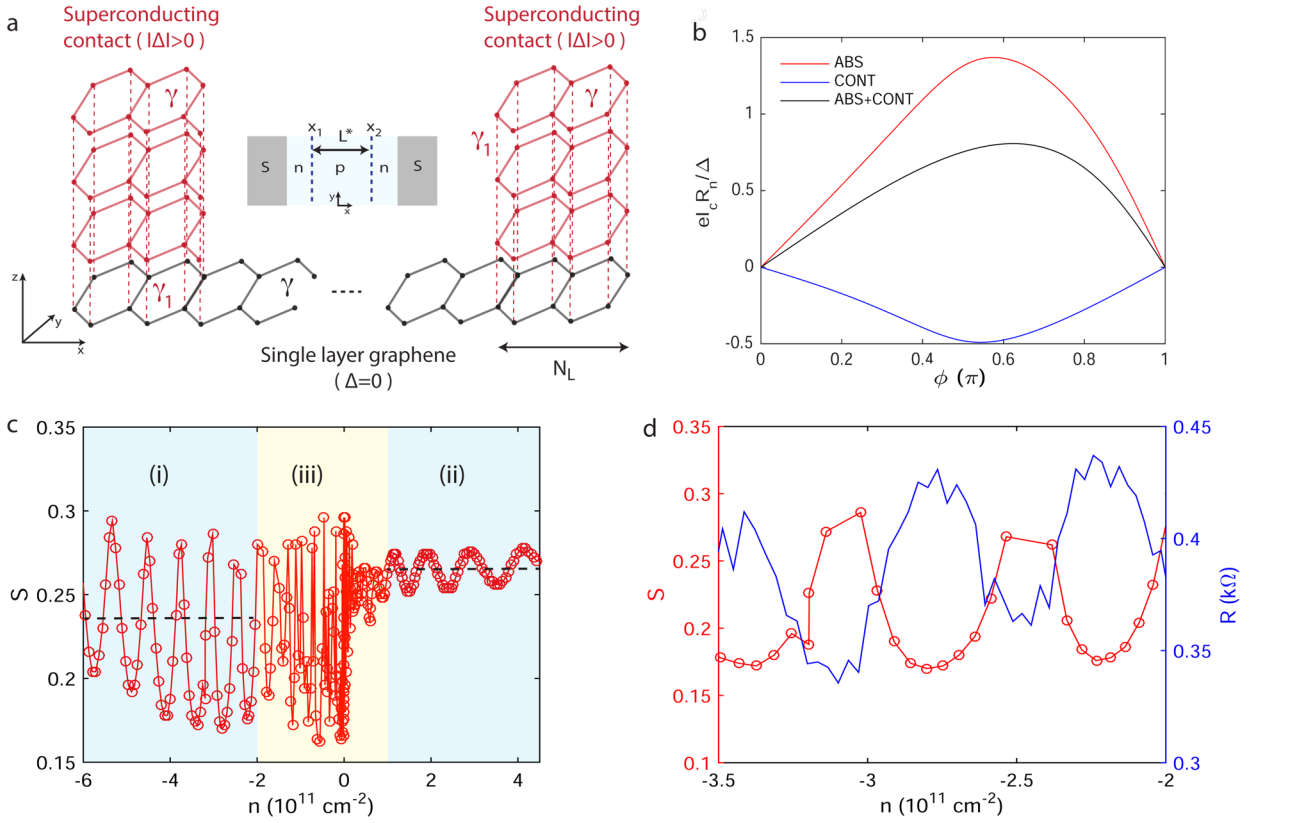

Figure 4. (a) The geometry of the system used in the calculations. The superconducting leads are attached in a top-contact geometry to the normal graphene sheet and overlap with the normal graphene sheet over N_L unit cells. γ denotes the nearest-neighbor intralayer hopping in the leads and in the graphene sheet, while γ_1 is the nearest-neighbor interlayer hopping. A periodic boundary condition is applied in the y-direction. (Inset) Top view of the system. Because of doping from the S contacts, the normal graphene region is assumed to be n-doped up to a distance x_1 (x_2) from the left (right) contact. The distance $L^* = x_2 - x_1$ is the effective cavity length which depends on the gate voltage applied to the junction. (b) The contribution of the ABSs (red) and continuum CONT (blue) to the total supercurrent (black) as a function of the phase difference for an n-doped junction ($n = 0.9 \times 10^{11}$ cm^{-2} and $L/\xi_0 = 0.73$). (c) The skewness S as a function of doping of the junction. The regimes i–iii indicated by the rectangles are further discussed in the text. Dashed lines show the average S in the p- and n-doped regime. (d) The skewness (red circles, left axis) and normal state resistance (blue, right axis) versus doping for strong p-doping of the junction.

compute the expected SQUID response (see SI for details of the simulations). These plots (solid lines) show an excellent agreement between simulations and experiment, thus confirming that the asymmetry of our SQUID is sufficient to reliably estimate the CPR of L-JJ. Furthermore, it shows that there are no significant effects of inductance in our measurements, which could potentially complicate the extraction of the CPR from $I_c(\Phi)$ in an asymmetric SQUID.[24]

To study the gate dependence of the CPR we fix V_R at +10 V (to maximize I_{cR}) and study the change in S with V_L (Figure 3a) for Dev1 and Dev2. The SI shows the $I_s(\phi)$ curves used to extract S. For both devices we find that S is larger on the n-side as compared to the p-side, showing a dip close to the CNP. We note that Dev2 allows us to probe the CPR up to a larger range on the n-side due to its larger geometric asymmetry (see SI for other measurements on Dev2). We expect the skewness to depend strongly on the total transmission through the graphene JJ, which should depend on (a) the number of conducting channels in the graphene, as well as (b) the transparency of the graphene-superconductor interface. The gate voltage V_L obviously changes the Fermi wave vector but it also changes the contact resistance,[25] which plays a significant role in determining S. This can be seen most clearly for Dev2 for high n-doping, where S saturates, despite the fact that I_{cL} continues to increase up to the largest measured density (see inset). At large p-doping, S also seems to saturate but a closer look (Figure 3b) shows that S oscillates in antiphase with the FP oscillations in resistance. This clearly indicates that in this regime the CPR is modulated by phase coherent interference effects similar to the FP oscillations that affect the total transmission.

We complement our measurements with a minimal theoretical model by solving the corresponding Bogoliubov–de Gennes (BdG) equations to calculate the CPR in graphene JJs. To set the stage, we note that SNS junctions can be characterized by the quasiparticle mean free path l_f in the normal (N) region and the coherence length $\xi_0 = \hbar v_F/\Delta$, where v_F is the Fermi velocity in N. In our devices $L \ll l_f$, that is, they are in the ballistic regime, and therefore we neglect impurity scattering in our calculations. Taking $v_F \approx 10^6$ m/s for graphene and $\Delta \approx 1.2$ meV for MoRe, one finds $\xi_0 = 548$ nm, which means that in our junctions $L \lesssim \xi_0$, that is, they are not in the strict short junction limit $L \ll \xi_0$. Consequently, the Josephson current is carried not only by discrete Andreev bound states (ABSs) but also by states in the continuum (CONT).[26−28] For this reason, we numerically solve the BdG equations using a tight-binding (TB) model (see Figure 4a) and a recently developed numerical approach[17,29] which handles the ABSs and states in the continuum on equal footing. The description of both the normal region and the superconducting terminals is

DOI: 10.1021/acs.nanolett.7b00097
Nano Lett. XXXX, XXX, XXX−XXX

based on the nearest-neighbor TB model of graphene.[30] The on-site complex pair-potential Δ is finite only in the superconducting terminals and changes as a step-function at the $N-S$ interface. The results presented here are calculated using the top-contact geometry (Figure 4a), a model with perfect edge contacts is discussed in the SI. As observed experimentally, we take into account n-doping from the superconducting contacts (see Figure 4a inset). If the junction is gated into hole-doping, a FP cavity is formed by the two n−p junctions in the vicinity of the left and right superconducting terminals. The length L^* of this FP cavity depends on the gate voltage,[4] for stronger hole-doping the n−p junctions shift closer to the contacts. For further details of the model see SI.

Turning now to the CPR calculations, Figure 4b shows separately the contribution of the ABS and the continuum to the supercurrent. Because $L \lesssim \xi_0$, the latter contribution is not negligible and affects both the value of the critical current and the skewness of the CPR. We note that our calculations can qualitatively reproduce the doping dependence of I_c (see SI), however the obtained values of I_c are about 2.5 times larger than the measurements (Figure 3a inset). The exact reason for this discrepancy is not known, but a similar disagreement between theory and experiment was also found in ref 4. Focusing now on the skewness, in Figure 4c we show the calculated skewness S as a function of the doping of the junction at zero temperature. We consider three regimes: (i) strongly p-doped junction; (ii) large n-doping, (iii) the region around the CNP. We start with the discussion of (i). It is well established that in this case the p−n junctions lead to FP oscillations in the normal resistance as well as in the critical current[3,4] of graphene JJs. Our calculations, shown in Figure 4d, indicate that due to FP interference the skewness also displays oscillations as a function of doping around an average value of $S \approx 0.23$. As already mentioned, similar oscillations are present in the normal state resistance R, however, we find that R oscillates in antiphase with the skewness. Compared to the measurements (Figure 3b), our calculations therefore reproduce the phase relation between the oscillations of the skewness and R and give a qualitatively good agreement with the measured values of the skewness. In the strong n-doped regime (case (ii) the calculated average skewness of $S = 0.27$ is larger than for p-doped junctions, and very close to the measured values. Small oscillations of S are still present in our results and they are due to the n−n′ interfaces, that is, the difference in the doping close to the contacts (for $x < x_1$ and $x > x_2$, see Figure 4a inset) and the junction region ($x_1 < x < x_2$), which enhances backscattering. Our calculations therefore predict smaller skewness for p-doped than for n-doped junctions. The enhancement of S in the n-doped regime can be clearly seen in the measurements of Figure 3a. We note that previous theoretical work,[16] which calculated the spatial dependence of the pairing amplitude self-consistently, predicted a skewness of $S \approx 0.15$ for n-doped samples with $L < \xi_0$, while a nonself-consistent calculation which took into account only the contribution of the ABS yielded $S \approx 0.42$.[16] The comparison of these results to ours and to the measurements suggest that the skewness may depend quite sensitively on the $S-N$ interface as well as on the L/ξ_0 ratio and that our approach captures the most important effects in these junctions. Finally, we briefly discuss the case (iii), where the measurements show a suppression of the skewness as the CNP is approached. The measured values of $S \sim 0.1$ are similar to those found in diffusive junctions[19] but are significantly lower than the theoretical prediction of $S = 0.26$ in the short junction limit[13] at the CNP. This suppression of S is not reproduced in our calculations, instead, we find rapid oscillations as the CNP is approached from the p-doped regime. This discrepancy is likely to be due to effects that are not included in our ballistic model, such as charged scatterers that are poorly screened in this regime, or scattering at the edges, which is more relevant at low densities when only a few open channels are present.

Finally, we study the effect of temperature on the CPR of these JJs. In Figure 5a, we compare the CPR in the n-doped

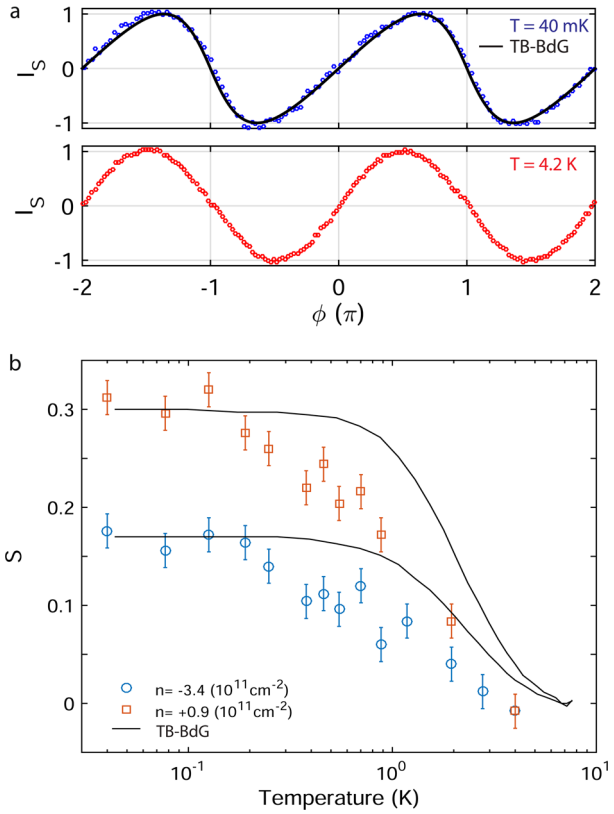

Figure 5. (a) CPR for $V_L = +1$ V ($n = 0.9 \times 10^{11}$ cm^{-2}) at 40 mK (upper curve) and 4.2 K (lower curve). Solid line shows the calculated CPR. A forward skewness is clearly seen in the curve at 40 mK but is absent at 4.2 K. (b) Variation of S with temperature for electron and hole doping. Increasing the temperature suppresses higher harmonics in the CPR, thereby reducing S until it vanishes near 4.2 K and the curves become sinusoidal. Black lines show the results of tight binding simulations.

regime ($V_L = +1$ V; $n = 0.9 \times 10^{11}$ cm^{-2}) at 40 mK and 4.2 K. One clearly sees that at 4.2 K the CPR is sinusoidal. This is consistent with our observation that the critical current modulation of the SQUID is nearly 100% at 4.2 K (Figure 1d), a condition which can only be achieved if the CPR is sinusoidal. Figure 5b shows the full temperature dependence of S for two representative values of electron and hole doping (see SI for the corresponding temperature dependence of the critical currents). The reduction in skewness with temperature is consistent with the thermal population of excited Andreev bound states and continuum states.[14,16,17,19] We compare our results with numerical estimates which take into account this effect, along with the temperature dependence of the pair potential (black curves in Figure 5b). While the qualitative behavior of both (experimental and numerical) curves are

DOI: 10.1021/acs.nanolett.7b00097
Nano Lett. XXXX, XXX, XXX−XXX

similar, the experimentally determined skewness reaches zero (sinusoidal CPR) faster than the numerics. At this point, it is difficult to ascertain the exact reason for this discrepancy but one possible explanation for this is that the induced superconducting gap in the graphene is somewhat smaller than the bulk MoRe gap, resulting in a faster decay.

In conclusion, we have used a fully gate-tunable graphene based SQUID to provide measurements of the current-phase relation in ballistic Josephson junctions made with encapsulated graphene. We show that the CPR is nonsinusoidal and can be controlled by a gate voltage. We complement our experiments with tight binding simulations to show that the junction length and nature of the superconductor−graphene interface play an important role in determining the CPR. We believe that the simplicity of our device architecture and measurement scheme should make it possible to use such devices for studies of the CPR in topologically nontrivial graphene Josephson junctions.

■ ASSOCIATED CONTENT

Supporting Information

The Supporting Information is available free of charge on the ACS Publications website at DOI: 10.1021/acs.nanolett.7b00097.

Device fabrication; additional data from other devices; magnetic field to phase conversion; quantifying inductance effects; RCSJ simulations; details of tight binding-Bogoliubov-de Gennes calculations (PDF)

■ AUTHOR INFORMATION

Corresponding Author

*E-mail: S.Goswami@tudelft.nl.

ORCID

J. L. Aguilera-Servin: 0000-0002-2862-8372

S. Goswami: 0000-0002-9095-4363

Notes

The authors declare no competing financial interest.

■ ACKNOWLEDGMENTS

We thank A. Geresdi and D. van Woerkom for useful discussions. S.G. and L.M.K.V. acknowledge support from the EC-FET Graphene flagship and the Dutch Science Foundation NWO/FOM. A.K. acknowledges funding from FLAG-ERA through project "iSpinText". P.R. acknowledges the support of the OTKA through the Grant K108676, the support of the postdoctoral research program 2015, and the support of the János Bolyai Research Scholarship of the Hungarian Academy of Sciences. K.W. and T.T. acknowledge support from the Elemental Strategy Initiative conducted by the MEXT, Japan and JSPS KAKENHI Grants JP26248061, JP15K21722, and JP25106006.

■ REFERENCES

(1) Efetov, D. K.; Wang, L.; Handschin, C.; Efetov, K. B.; Shuang, J.; Cava, R.; Taniguchi, T.; Watanabe, K.; Hone, J.; Dean, C. R.; Kim, P. *Nat. Phys.* **2015**, *12*, 328−332.

(2) Lee, G. H.; Huang, K. F.; Efetov, D. K.; Wei, D. S.; Hart, S.; Taniguchi, T.; Watanabe, K.; Yacoby, A.; Kim, P. *Nat. Phys.* **2017**, in press DOI: 10.1038/nphys4084.

(3) Calado, V. E.; Goswami, S.; Nanda, G.; Diez, M.; Akhmerov, A. R.; Watanabe, K.; Taniguchi, T. M. K.; Vandersypen, L. M. K. *Nat. Nanotechnol.* **2015**, *10*, 761−764.

(4) Shalom, M. B.; Zhu, M. J.; Fal'ko, V. I.; Mishchenko, A.; Kretinin, A. V.; Novoselov, K. S.; Woods, C. R.; Watanabe, K.; Taniguchi, T.; Geim, A. K.; Prance, J. R. *Nat. Phys.* **2015**, *12*, 318.

(5) Allen, M. T.; Shtanko, O.; Fulga, I. C.; Akhmerov, A. R.; Watanabe, K.; Taniguchi, T.; Jarillo-Herrero, P.; Levitov, L. S.; Yacoby, A. *Nat. Phys.* **2015**, *12*, 128−133.

(6) Amet, F.; Ke, C. T.; Borzenets, I. V.; Wang, J.; Watanabe, K.; Taniguchi, T.; Deacon, R. S.; Yamamoto, M.; Bomze, Y.; Tarucha, S.; Finkelstein, G. *Science* **2016**, *352*, 966−969.

(7) Borzenets, I. V.; Amet, F.; Ke, C. T.; Draelos, A. W.; Wei, M. T.; Seredinski, A.; Watanabe, K.; Taniguchi, T.; Bomze, Y.; Yamamoto, M.; Tarucha, S.; Finkelstein, G. *Phys. Rev. Lett.* **2016**, *117*, 237002.

(8) Murani, A.; Kasumov, A.; Sengupta, S.; Kasumov, Y.; Volkov, V. T.; Khodos, I.; Brisset, F.; Delagrange, R.; Chepelianskii, A.; Deblock, R.; Bouchiat, H.; Guéron, S. 2016, arXiv:1609.04848, accessed January 9, 2017.

(9) Spanton, E. M.; Deng, M.; Vaitiekėnas, S.; Krogstrup, P.; Nygård, J.; Marcus, C. M.; Moler, K. A. 2017, arXiv:1701.01188, accessed January 9, 2017.

(10) Miyazaki, H.; Kanda, A.; Ootuka, Y. *Phys. C* **2006**, *437-438*, 217−219.

(11) Della Rocca, M. L.; Chauvin, M.; Huard, B.; Pothier, H.; Esteve, D.; Urbina, C. *Phys. Rev. Lett.* **2007**, *99*, 127005.

(12) Fu, L.; Kane, C. L. *Phys. Rev. B: Condens. Matter Mater. Phys.* **2009**, *79*, 161408.

(13) Titov, M.; Beenakker, C. W. J. *Phys. Rev. B: Condens. Matter Mater. Phys.* **2006**, *74*, 041401.

(14) Hagymási, I.; Kormányos, A.; Cserti, J. *Phys. Rev. B: Condens. Matter Mater. Phys.* **2010**, *82*, 134516.

(15) Black-Schaffer, A. M.; Doniach, S. *Phys. Rev. B: Condens. Matter Mater. Phys.* **2008**, *78*, 024504.

(16) Black-Schaffer, A. M.; Linder, J. *Phys. Rev. B: Condens. Matter Mater. Phys.* **2010**, *82*, 184522.

(17) Rakyta, P.; Kormányos, A.; Cserti, J. *Phys. Rev. B: Condens. Matter Mater. Phys.* **2016**, *93*, 224510.

(18) San-Jose, P.; Lado, J.; Aguado, R.; Guinea, F.; Fernández-Rossier, J. *Phys. Rev. X* **2015**, *5*, 041042.

(19) English, C. D.; Hamilton, D. R.; Chialvo, C.; Moraru, I. C.; Mason, N.; Van Harlingen, D. J. *Phys. Rev. B: Condens. Matter Mater. Phys.* **2016**, *94*, 115435.

(20) Lee, G. H.; Kim, S.; Jhi, S. H.; Lee, H. J. *Nat. Commun.* **2015**, *6*, 6181.

(21) Girit, Ç.; Bouchiat, V.; Naaman, O.; Zhang, Y.; Crommie, M. F.; Zettl, A.; Siddiqi, I. *Nano Lett.* **2009**, *9*, 198.

(22) Girit, Ç.; Bouchiat, V.; Naaman, O.; Zhang, Y.; Crommie, M. F.; Zettl, A.; Siddiqi, I. *Phys. Status Solidi B* **2009**, *246*, 2568.

(23) Golubov, A. A.; Kupriyanov, M. Y.; Il'ichev, E. *Rev. Mod. Phys.* **2004**, *76*, 411−469.

(24) Fulton, T. A.; Dunkleberger, L. N.; Dynes, R. C. *Phys. Rev. B* **1972**, *6*, 855−875.

(25) Wang, L.; Meric, I.; Huang, P. Y.; Gao, Q.; Gao, Y.; Tran, H.; Taniguchi, T.; Watanabe, K.; Campos, L. M.; Muller, D. A.; Guo, J.; Kim, P.; Hone, J.; Shepard, K. L.; Dean, C. R. *Science* **2013**, *342*, 614−617.

(26) Svidzinsky, A. V.; Antsygina, T. N.; Bratus, E. N. *J. Low Temp. Phys.* **1973**, *10*, 131.

(27) Giuliano, D.; Affleck, I. *J. Stat. Mech.: Theory Exp.* **2013**, *2013*, P02034.

(28) Perfetto, E.; Stefanucci, G.; Cini, M. *Phys. Rev. B: Condens. Matter Mater. Phys.* **2009**, *80*, 205408.

(29) The numerical calculations were performed with the EQuUs software, see http://eqt.elte.hu/equus/home, accessed January 9, 2017.

(30) Wakabayashi, K.; Fujita, M.; Ajiki, H.; Sigrist, M. *Phys. Rev. B: Condens. Matter Mater. Phys.* **1999**, *59*, 8271−8282.

■ NOTE ADDED AFTER ASAP PUBLICATION

This paper published ASAP on 5/11/2017. Figure 3 was corrected and the revised version was reposted on 5/16/2017.

DOI: 10.1021/acs.nanolett.7b00097
Nano Lett. XXXX, XXX, XXX−XXX

Supplementary Information: Current-phase relation of ballistic graphene Josephson junctions

G. Nanda,[†] J. L. Aguilera-Servin,[†,‡] P. Rakyta,[¶] A. Kormányos,[§] R. Kleiner,[‖] D. Koelle,[‖] K. Watanabe,[⊥] T. Taniguchi,[⊥] L. M. K. Vandersypen,[†,#] and S. Goswami[*,†,#]

†Kavli Institute of Nanoscience, Delft University of Technology, 2600 GA Delft, The Netherlands.

‡Institute of Science and Technology Austria, Am Campus 1, A-3400 Klosterneuburg, Austria.

¶Department of Physics of Complex Systems, Eötvös University, Pázmány Péter Sétány 1/A, H-1117 Budapest, Hungary.

§Department of Physics, University of Konstanz, D-78464 Konstanz, Germany.

‖Physikalisches Institut and Center for Quantum Science (CQ) in LISA⁺, Eberhard Karls Universität Tübingen, Auf der Morgenstelle 14, D-72076 Tübingen, Germany.

⊥National Institute for Materials Science, 1-1 Namiki, Tsukuba, 305-0044, Japan.

#QuTech, Delft University of Technology, 2600 GA Delft, The Netherlands.

E-mail: S.Goswami@tudelft.nl

1. Device Fabrication

Graphene flakes are exfoliated onto silicon chips with 90 nm SiO_2. Next, h-BN is exfoliated separately on a glass slide covered by a 1-cm^2 piece of PDMS coated with an MMA/MAA copolymer layer. This glass slide is baked for 20 minutes on a hot plate at 120°C, prior to h-BN exfoliation. The glass slide is mounted on a micromanipulatior in a home-built set-up (similar to Ref[1]) equipped with a heating stage. Next, a h-BN flake on the slide is aligned with the target graphene and the substrate is heated to 90°C. The flakes are brought into contact, after which the glass slide is released smoothly such that the graphene flake is picked up by the h-BN flake on the glass slide. Finally, the graphene/h-BN stack is transferred onto another h-BN flake (exfoliated onto a silicon chip with 285 nm SiO_2), at a temperature of 80°C.

The fabrication flow is outlined in Figure S1. First MoRe contacts are made to the stack via an etch fill technique[2] using standard e-beam lithography. The sample is plasma-etched for 1 min in a flow of 40/4 sccm CHF_3/O_2 with 60 W power, and 80μbar pressure. After etching, we immediately sputter ~70 nm MoRe using a DC plasma with a power of 100 W in an Argon atmosphere. Next, the MoRe lift-off is completed in hot (54°C) acetone for about 3-4 hours. The two JJs are shaped using another e-beam lithography in which the intended graphene geometry is defined via a PMMA/hydrogen-silsesquioxane (HSQ) mask, followed by CHF_3/O_2 etching. In order to isolate the contacts from the top gate, we use ~170 nm of

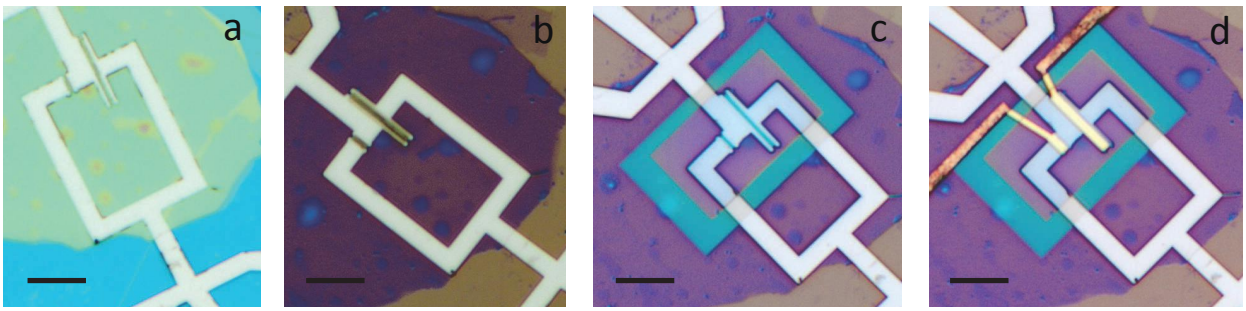

Figure S1: Optical images of device after (a) MoRe deposition, (b) shaping of the graphene, (c) dielectric (HSQ) deposition, and (d) deposition of top gates. The scale bar for all images is 5 μm.

HSQ as a dielectric. Finally, top gates are fabricated by e-beam evaporation of 5nm Cr + 120 nm Au, and subsequent lift off in hot acetone.

2. Ballistic transport in Dev2

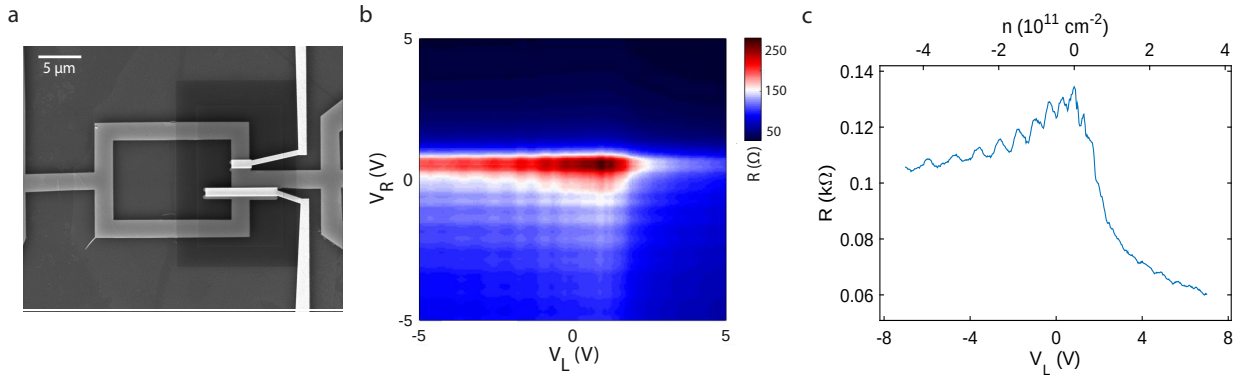

Figure S2: (a) Scanning electron micrograph of Dev2 from main text. The left junction (L_{JJ}) is 0.4 μm long (L) and 8 μm wide (W), while the right junction (R_{JJ}) is 0.4 μm long and 2 μm wide. (b) Resistance map as a function of V_L and V_R at 4.2 K, demonstrating independent control of carrier type and density in left and right JJ, respectively. (c) Resistance vs V_L (while keeping V_R fixed at CNP of R-JJ) showing Fabry-Pérot oscillations in resistance.

3. Temperature dependence of critical current

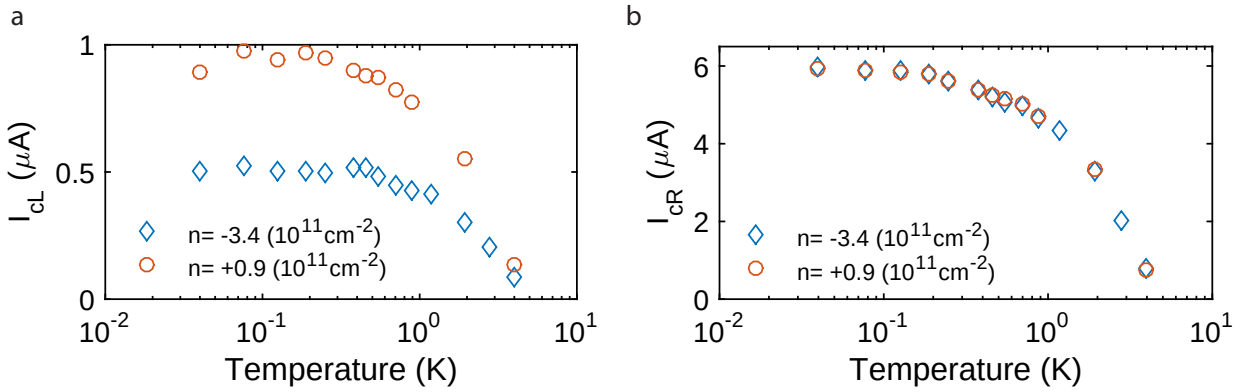

Figure S3: Temperature dependence of the (a) left and (b) right JJs assosciated with the data shown in Figure 5b of the main text.

4. Magnetic field to phase conversion

In the main text we pointed out that one must take care in converting the flux-periodic oscillations of the critical current of the SQUID $I_c(\Phi)$ to the CPR of L-JJ $I_s(\phi)$. Figure S4 shows how this is done. We start with the upper plot in Figure 2a of the main text, which is shown here again for convenience (Figure S4a). We then subtract a constant background (I_{cR}) about which the curve oscillates and normalize it with respect to the oscillation amplitude (I_{cL}). Also, the flux is converted to phase by $\phi^* \to 2\Phi/\Phi_0$. This is not the true phase ϕ for two important reasons. Firstly, the zero of the magnetic field is not known precisely. Secondly, the flux to phase conversion is only possible up to a constant offset, which is determined by the CPR of R-JJ (which is a-priori unknown). In order obtain the CPR we then offset the curve in Figure S4b along the ϕ^* axis such that the supercurrent at zero phase difference is zero, which finally gives us the CPR. We note that this procedure is only valid

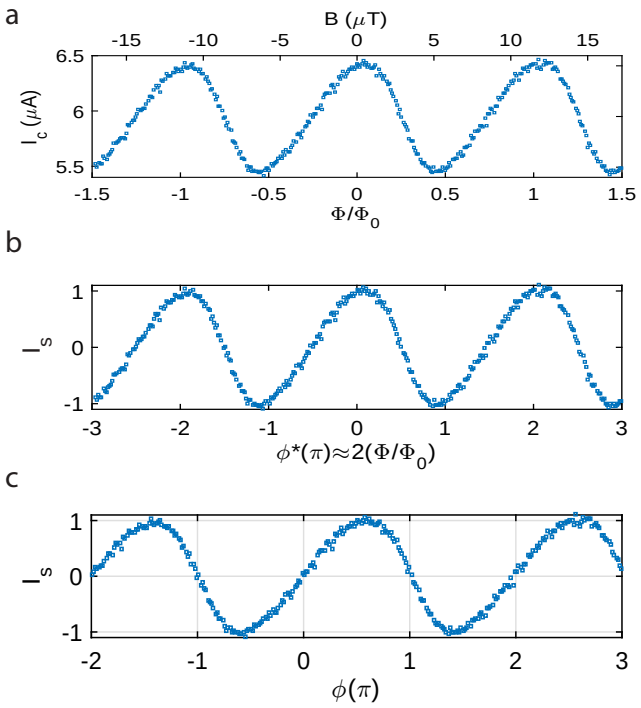

Figure S4: (a) The variation of I_c as a function of magnetic field B for $V_L = -4$ V and $V_R = +10$ V. (b) The curve in (a) replotted after converting flux Φ to phase ϕ^*, and rescaling I_c to $I_s = (I_c - I_{cR})/I_{cL}$. (c) Curve in (b) offset along the ϕ^*-axis to ensure that $I_s(0) = 0$, thus giving the true phase ϕ axis.

for systems where $I_s(\phi) = -I_s(-\phi)$ and $I_s(0) = 0$, both of which are reasonable assumptions for our graphene JJs.

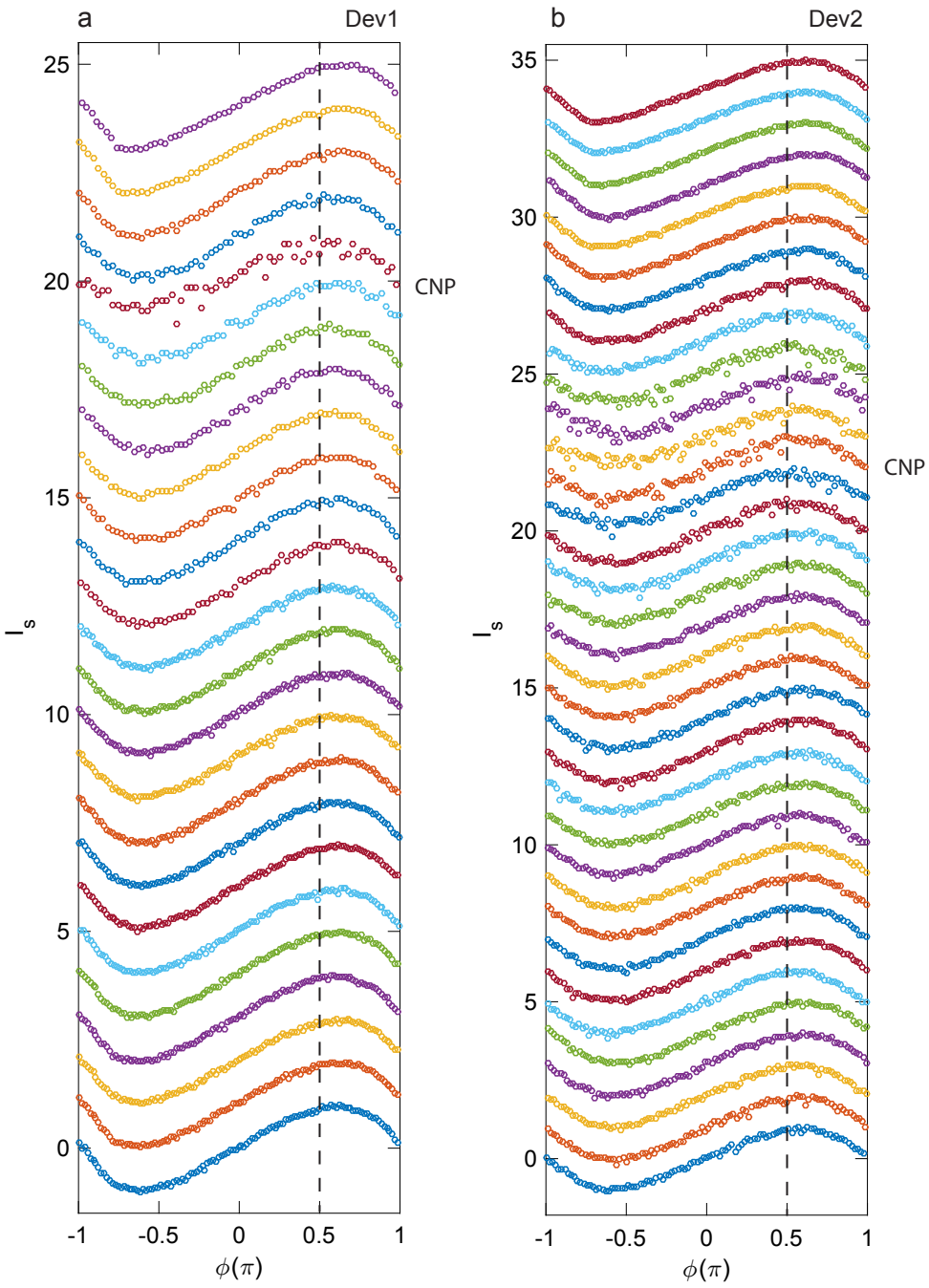

Figure S5: All measured CPR (I_s vs. ϕ) plots for (a) Dev1 and (b) Dev2 used to extract the skewness in Figure 3a of the main text. The plots have been offset by 1, with the lowest (highest) plots corresponding to large p (n) doping. The plot corresponding to the CNP has also been indicated.

5. Eliminating inductance effects

In an asymmetric SQUID inductance effects can give rise to skewed $I_c(\Phi)$ curves. It is therefore important to establish that such effects do not dominate the response of the SQUIDs described in this study. To do so, we first provide some qualitative arguments which make it evident that the skewness arises only from a non-sinusoidal CPR. Furthermore, we extract the loop inductance of our SQUID, use it as an input for the RCSJ model and confirm that (within our experimental resolution) the inductance does not play an important role in determining the shape of the $I_c(\Phi)$ curves, and hence does not affect our ability to measure the CPR.

Large asymmetry

We have shown that for large asymmetry (i.e., $I_{cR} >> I_{cL}$), we probe the CPR of L-JJ. We define the asymmetry parameter $a_i = (I_{cR} - I_{cL})/(I_{cR} + I_{cL})$. Figure S6a shows three traces at T = 40 mK, where $I_{cL} \approx 0.5$ μA is kept fixed and I_{cR} is varied from 6 μA (black trace, $a_i \approx 0.83$) to 2.8 μA (red trace, $a_i \approx 0.78$). Figure S6b shows that all three curves collapse despite the fact that the maximum critical current ($I_{max} = I_{cR} + I_{cL}$) changes by a factor of two. If the skewness was dominated by inductance effects, we would have not expected this collapse, since the screening parameter $\beta_L = I_{max}L/\Phi_0$ increase by a factor of two (going from the red trace to the blue trace). In other words, the combined effect of large asymmetry and inductance should have resulted in a larger skewing of the black trace (maximum β_L and a_i) as compared to the red one.

Intermediate asymmetry

We have shown in the main text (Figure 5) that the skewness of the CPR decreases with increasing temperature, resulting in a sinusoidal CPR at 4.2 K. One might argue that this is consistent with inductance effects, whereby an increase in temperature reduces the critical

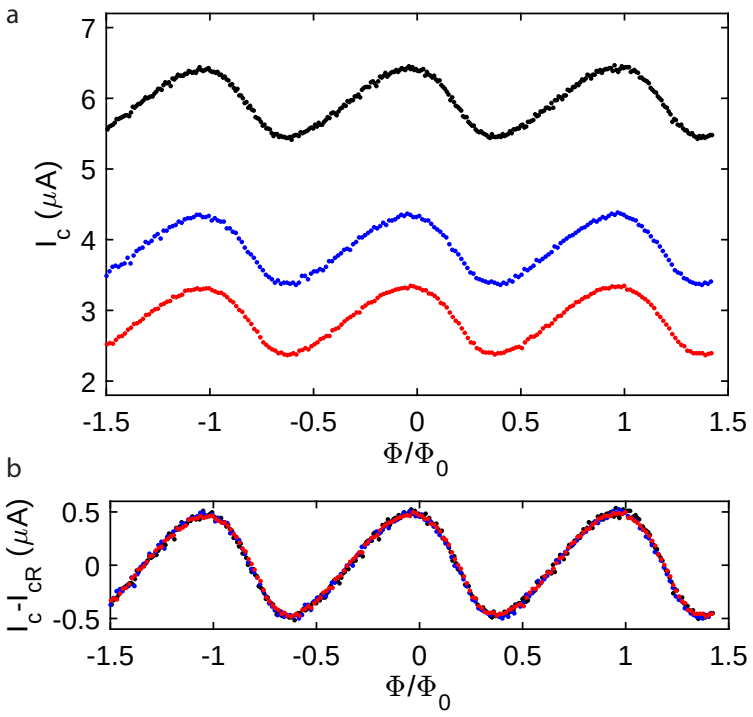

Figure S6: (a) $I_c(\Phi)$ plots with fixed I_{cL}, but varying I_{cR}, as shown earlier in Figure 2a of the main text. (b) The curves in (a), now plotted as $(I_c - I_{cR})$ vs. Φ. Collapse of the curves shows that the skewness does not depend on I_c, and hence represents the CPR of L-JJ.

currents and hence β_L. To eliminate this possibility, we compare $I_c(\Phi)$ at 40 mK and 4.2 K. Figure S7a,b show two such data sets. In each case the gate voltages were tuned such that both I_{max} and a_i were roughly the same for both temperatures. We see that at 40 mK the curves are noticeably skewed as compared to 4.2 K. The asymmetry here is not sufficient to directly extract the CPR, but it clearly demonstrates that the non-sinusoidal CPR also manifests itself in skewed $I_c(\Phi)$ curves at intermediate asymmetry. We note that this argument is made stronger by the fact that the inductance at 4.2 K should in fact be larger than that at 40 mK, since the inductance of the MoRe loop is dominated by kinetic inductance, which increases at higher temperatures. In other words, one would expect inductance related effects to be enhanced at higher temperatures, rather than become suppressed.

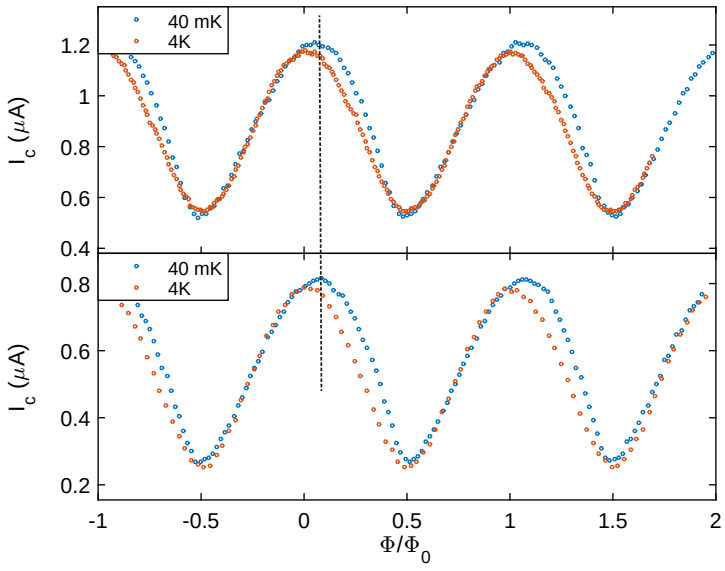

Figure S7: $I_c(\Phi)$ plots at $I_{max} \approx 1.2$ μA (upper) and ≈ 0.8 μA (lower) for low asymmetries of $a_i = 0.45$, $a_i = 0.33$ respectively. The curves at 40 mK are skewed (indicated by position of dashed line), while those at 4.2 K are not.

Estimating the loop inductance

Figure S8a shows $I_c(\Phi)$ measurements of an asymmetric SQUID at 4.2 K, where we have established that the CPR is sinusoidal. The position of maximum I_c for positive and negative current bias are offset along the flux axis due to self-flux effects.[3] This shift is given by: $\Delta\Phi = 2L(I_{cR} - I_{cL})$, where I_{cR} and I_{cL} are the critical current of right and left junction respectively. Figure S8b shows the variation of $\Delta\Phi$ with I_{max}. These values are obtained

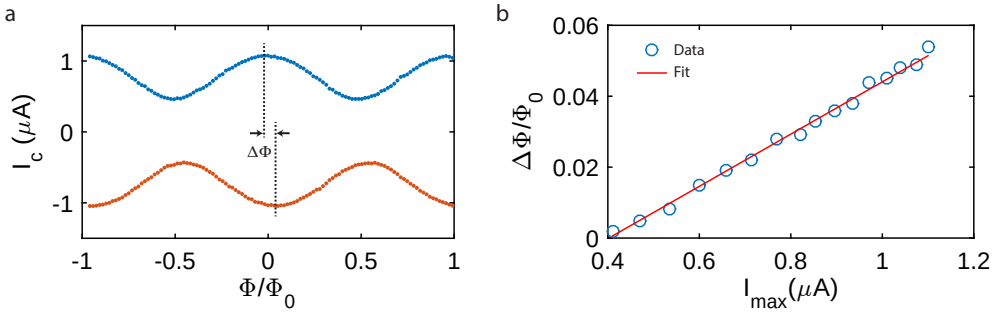

Figure S8: (a) $I_c(\Phi)$ curves for an asymmetric SQUID. (b) Variation of $\Delta\Phi$ with I_{max}. Here I_{cL} is kept fixed, while I_{cR} is varied. Blue circles are the experimentally obtained values of $\Delta\Phi$ and the red line is a linear fit to the data.

by keeping $I_{cL} \approx 0.2$ μA fixed and varying I_{cR} from 0.2 μA (symmetric configuration) to 0.9 μA (highly asymmetric). Since $\partial\Delta\Phi/\partial I_{cR} = L$, a linear fit (red line) allow us to extract $L \approx 152$ pH. Since MoRe is a highly disordered superconductor, its inductance is dominated by the kinetic inductance and the low temperature inductance $L(0) = L(T)[1 - (T/T_c)^2]$, giving $L \approx 110$ pH at $T = 40$ mK. We use this inductance to compare our experiments with the RCSJ simulations described below.

6. RCSJ Model

To model the asymmetric SQUID we consider the circuit shown in Figure S9. The Josephson junctions are described by the resistively and capacitively shunted junction (RCSJ) model[4,5] by Josephson currents with phases δ_L and δ_R and amplitudes $I_{cL} = I_c(1 - a_i)$ and $I_{cR} = I_c(1 + a_i)$, resistors R_L and R_R , and capacitors C_L and C_R. The Josephson currents are given by $I_L = I_c(1 - a_i) \cdot f_L(\delta_L)$ and $I_R = I_c(1 + a_i) \cdot f_L(\delta_L)$, where $f_i(\delta_i)$ are the normalized current-phase relations of the left and right JJ, respectively. The Nyquist noise arising from the two resistors is described by two independent current noise sources I_{NL} and I_{NR} having white spectral power densities $4k_BT/R_L$ and $4k_BT/R_R$, respectively. The two arms

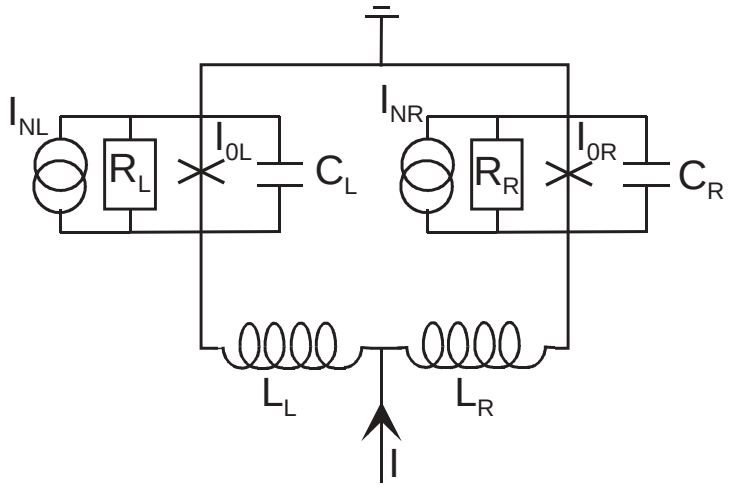

Figure S9: Circuit diagram of the asymmetric SQUID.

of the SQUID loop have inductances L_L and L_R . The total inductance L is the sum of the geometric (L_g) and the kinetic (L_k) inductance. The loop is biased with a current I, and a flux Φ is applied to the loop.

In the following we are interested only in static solutions and normalize currents by I_c. The currents i_L and i_R through the left (right) arm of the SQUID are then given by:

$$i_R = (1 + a_i) \cdot f_R(\delta_R). \tag{1}$$

$$i_L = (1 - a_i) \cdot f_L(\delta_L). \tag{2}$$

Assuming for simplicity that $L_L = L_R$ (a reasonable assumption based on our device geometry) the normalized circulating current j is given by:

$$j = \frac{i_R - i_L}{2} = \frac{1}{\beta_L}\Big(\frac{\delta_L - \delta_R}{\pi} - 2\Phi/\Phi_0\Big). \tag{3}$$

and the maximum current across the SQUID is $i_{cR} + i_{cL}$. From Equation 3 we obtain

$$\delta_L = 2\pi\Phi/\Phi_0 + \delta_R + \pi\beta_L\frac{i_R - i_L}{2}. \tag{4}$$

Let us consider the case $a_i >> 0$, i.e., the right junction has a much larger critical current than the left one. As we will see, in this case the modulation of the SQUID critical current reflects the CPR of the left junction, provided that $\beta_L << 1$.

$$i = i_R + i_L = (1 + a_I) \cdot f_R(\delta_R) + (1 - a_i) \cdot f_L(\delta_L). \tag{5}$$

From Equation 4, for $\beta_L << 1$, we obtain $\delta_L \approx 2\pi\Phi/\Phi_0 + \delta_R$. Thus

$$i = i_R + i_L = (1 + a_I) \cdot f_R(\delta_R) + (1 - a_i) \cdot f_L(2\pi\Phi/\Phi_0 + \delta_R). \tag{6}$$

Let us assume that $i > 0$. Then the task is to maximize i with respect to δ_R, to obtain $i_{c,SQUID}$ vs Φ/Φ_0. If the critical current of the right JJ is much bigger than the critical current of the left JJ, the value of δ_R will be close to the value δ_R^0 where the CPR of the right JJ has its maximum. We thus Taylor expand:

$$f_R(\delta_R) \approx f_R(\delta_R^0) + \frac{1}{2}\frac{d^2 f_R}{d\delta_R^2}\bigg|_{\delta_R^0} (\delta_R - \delta_R^0)^2 + ... \tag{7}$$

Note that in Equation 7 the first derivative of f_R is zero, because we look for the maximum of this CPR. If the second derivative (< 0) is reasonably peaked, δ_R will be very close to δ_R^0 and we obtain:

$$i_{c,SQUID} \approx (1+a_i)\cdot f_R(\delta_R^0) + (1-a_i)\cdot f_L(2\pi\Phi/\Phi_0 + \delta_R^0) = const + (1-a_i) f_L(2\pi\Phi/\Phi_0 + \delta_R^0). \tag{8}$$

That means that $i_{c,SQUID}$ vs. Φ/Φ_0 probes the CPR of the left JJ up to a phase shift δ_R^0 . f_L can be evaluated further if one assumes that $f_L = 0$ at $\delta_L = 0$ and that $\min(f_L) = -\max(f_L)$.

In Figure 2a of the main text we have compared our experiments with a full RCSJ simulation, as described above. These simulations involve no free parameters since we use the experimentally determined inductance, asymmetry (a_i), and CPR of L-JJ $f_L(\delta_L)$ as input parameters. For simplicity, the numerical plots were generated assuming a sinusoidal CPR for the reference junction R-JJ, shown as the blue curve in the Figure S10a. The red curve shows how $I_c(\Phi)$ changes when R-JJ is assumed to have a non-sinusoidal CPR (with a functional form similar to that extracted for L-JJ). The only effect this has is to offset the simulated curves along the flux axis. This is a consequence of the fact that δ_R^0 (as described above) is different for the two cases. However, we see in Figure S10b that these two cases perfectly overlap with an appropriate offset along the flux axis. This confirms the fact that an incomplete knowledge of the CPR of R-JJ is (in practice) equivalent to

an unknown offset in magnetic field, and therefore does not affect our ability to accurately determine the functional form of the CPR of L-JJ. The green curve in Figure S10a is a simulation with $\beta_L = 0.01$ (i.e., in the limit where the loop inductance is negligible). Looking carefully at Figure S10b shows that this $I_c(\Phi)$ has a slightly different shape as compared to the blue/red curves. However, this difference is well within the error bars for our estimation of the skewness, and we can conclude that the functional form of the $I_c(\Phi)$ curves is not dominated by the inductance effects, but by the non-sinusoidal CPR of L-JJ. This is in agreement with the conclusions drawn from more qualitative arguments presented in the previous section.

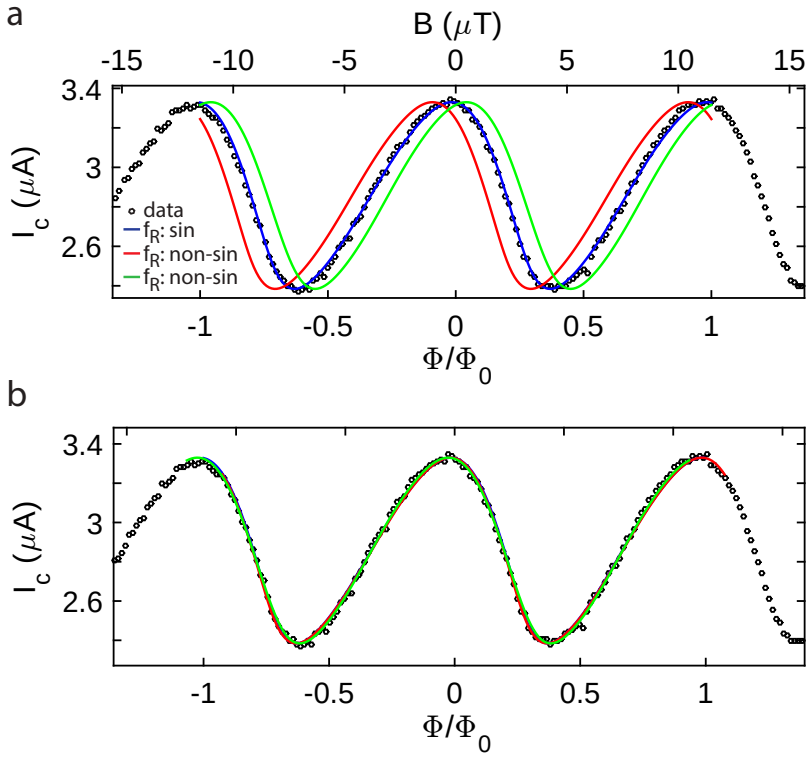

Figure S10: (a) Experimental $I_c(\Phi)$ (black) along with RCSJ simulations for a SQUID with $a_i = 0.83$. The blue (red) curve corresponds to a sinusoidal (non-sinusoidal) CPR f_R for the reference junction R-JJ, with the experimentally determined $\beta_L = 0.34$. The green curve shows the result for $\beta_L = 0.01$. The data has been offset along the flux axis to match the blue curve. (b) Same as (a), but with the red and green curves shifted along the flux axis.

7. Tight Binding-Bogoliubov-de Gennes Calculations

Details of the theoretical model

In this Section we provide further details of the theoretical model that we used in our numerical calculations. As it will be clear from the following discussion, we found that in order to obtain a good qualitative agreement with the measurements, a realistic and detailed model of the Josephson junction, especially the interface between the superconductor and the normal regions, is needed.

We assume that the graphene flake which serves as a weak link is perfectly ballistic and scattering processes only occur at the interfaces between regions of different doping in the normal part of the junction or between the superconductor and the normal region. The normal (N) and superconducting (S) regions are of the same width in our calculations. This allows us to use periodic boundary conditions perpendicular to the transport direction. The transverse momentum q_n is a good quantum number and the DC Josephson current can be calculated as a sum over all q_n:

$$I_J(\Delta\phi) = \sum_n I_J(q_n, \Delta\phi) \ , \tag{9}$$

where $I_J(q_n, \Delta\phi)$ is the momentum resolved Josephson current calculated for a specific transverse momentum q_n via the contour integral method developed recently in Reference.[6] For wide junctions and high dopings, when there are many transverse momenta, the exact form of the boundary conditions is not important and therefore we used the infinite mass boundary condition to obtain q_n: $q_n = \left(n + \frac{1}{2}\right) \frac{\pi}{W}$, where $n = 0, 1, 2, \ldots$ and W is the width of the junction.

The description of both the N region and the S terminals is based on the nearest-neighbour

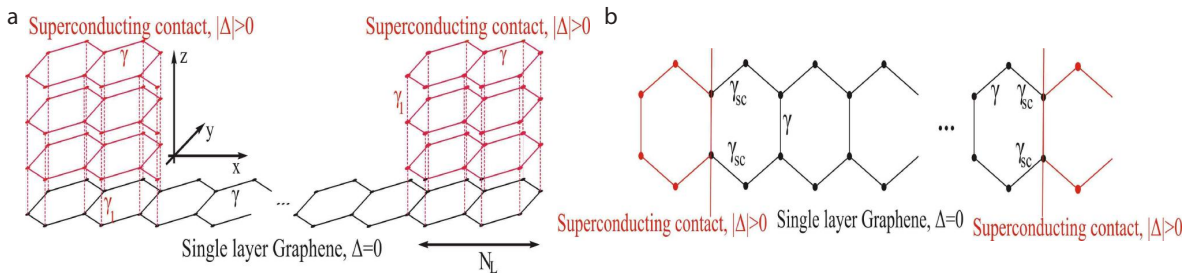

Figure S11: (a) The geometry of the top contacted superconductor-graphene-superconductor junction. N_L is the number of unit cells under the superconducting contacts in the x direction, (b) The side-contacted geometry. The interface resistance between the S and regions is modelled by a hopping $\gamma_{sc} < \gamma$. In both geometries the lattice is translational invariant in the y direction

tight-binding model of graphene[7]

$$\hat{H} = \sum_i U_i c_i^\dagger c_i - \sum_{\langle ij \rangle} \gamma c_i^\dagger c_j + h.c. \tag{10}$$

where U_i is the on-site energy on the atomic site i, $\gamma = 2.97\,\mathrm{eV}$ is the hopping amplitude between the nearest-neighbor atomic sites $\langle ij \rangle$ in the graphene lattice, and $c_i^\dagger$ (c_i) is a creation (annihilation) operator for electrons at site i. We considered two junction geometries. Most of our results were obtained using the top-contact geometry, which is shown in Figure 4(a) of the main text and for convenience repeated here in Figure S11(a). The S terminals are described by vertically stacked graphene layers (AA stacking) where the inter-layer hopping is given by $\gamma_1 = 0.6\,\mathrm{eV}$. The same inter-layer hopping γ_1 was also used between the S terminals and the N region. The S leads are coupled to the normal graphene sheet over N_L unit cells. The result do not depend strongly on the exact value of N_L, therefore we used $N_L = 10$ in our calculations.

To mimic metallic leads with many open channels, the S terminals are highly n-doped. This is described by an on-site potential U_n and we used $U_n = 350\,\mathrm{meV}$ in our calculations. For high n-doping of the N region we calculated an average transparency of $Tr = 0.82$ for the junction, see the Supplementary of Reference[8] for the precise definition of Tr. We find that the calculated Tr does not depend very sensitively on the precise value U_n and γ_1 because

most of the backscattering taking place at the interface of the S leads and the N region is due to a "geometric" effect: the electron trajectories have to turn at right angle to arrive from the lead into the N region. Moreover, we find that for $Tr = 0.82$ the calculated dependence of the normal state resistance R_n on the doping of the N region agrees qualitatively well with the measurements where the right JJ was kept at the charge neutrality point [c.f. Figure 1(c) in the main text and Figure S15(a) below]. (We did not try to achieve quantitative agreement for R_n because in the experiments the resistance of the two junctions are always measured in parallel, whereas we used single junctions in the calculations.)

As shown in Figure S11(b) and discussed further later on, we have also made calculations using the side-contact geometry. For both geometries we used open boundary conditions for the leads in the transport direction (which is the z direction in top-contacted geometry and the x direction in the side-contacted one, see Figure S11).

In contrast to the S leads, which are always n-doped in our calculations, the normal region of the JJ can be either n or p doped depending on the gate voltage. This is modeled by a doping potential U_p. Experimentally, it was shown that the superconducting terminals n-dope the normal region of the JJ.[2,8] This n-doped region extends to a distance x_1 ($L_0 - x_2$) from the left (right) terminal, where L_0 is the distance between the two S leads. The potential profile in the junction can be therefore either npn or $nn'n$. The exact value of the x_1 and x_2, and hence the cavity length $L^* = x_2 - x_1$, however, depends on the gating of the JJ. In the npn regime, where clear FP oscillations can be measured in the normal state resistance R_n in our devices, we extracted the experimental cavity length using the relation $L^*_{exp} \approx 2\sqrt{\pi n}/\delta n$, where δn is the density difference between consecutive peaks in R_n.[9]

The results of this analysis are summarized in Figure S12. We find that $L^*_{exp} \approx 310\,\mathrm{nm}$ is roughly constant for $n < -1.8 \times 10^{11}\mathrm{cm}^{-2}$, but it decreases for densities approaching the CNP. In order to extract the theoretical cavity length L^* for $n > -1.8 \times 10^{11}\mathrm{cm}^{-2}$, we fitted

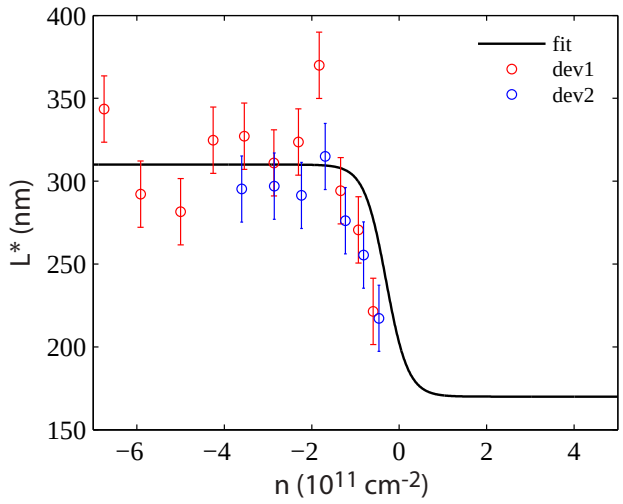

Figure S12: The experimental cavity length L^*_{exp} vs doping (symbols) and the fitting function used to obtain the L^* in our calculations (solid line).

the experimental results by the function

$$L^*(U_p) = \frac{L^*_{exp} - L_{nn'n}}{1 + \exp\left[\beta(n - n_0)\right]} + L_{nn'n}. \tag{11}$$

Here $L_{nn'n}$ is the cavity length for strongly n doped junctions which could not be determined from the R_n measurements, therefore we used $L_{nn'n} = 170\,\text{nm}$. As mentioned above, a good qualitative agreement between the calulated and measured normal state resistance is achieved using this value of $L_{nn'n}$. We have also checked that for $L_{nn'n} \gtrsim 160\,\text{nm}$ the calculation results do not depend strongly on the exact value of $L_{nn'n}$. The two fitting parameters in Eq. (11) are β and n_0 and we found $\beta = 4.0$ and $n_0 = -0.3$, see Figure S12. Once L^* is determined, the parameters x_1 and x_2 are given by $x_1 = \frac{L_0 - L^*(U_p)}{2}$ and $x_2 = L_0 - x_1$. The total potential profile along the junction, which describes the smooth transition between the highly doped regions ($x < x_1$ and $x > x_2$) and the central part of the junction ($x_1 \le x \le x_2$) is modeled by

$$U(x) = U_n + \frac{U_p - U_n}{2}\left(\tanh\left(\frac{x - x_1}{l_{tr}}\right) - \tanh\left(\frac{x - x_2}{l_{tr}}\right)\right). \tag{12}$$

where the parameter l_{tr} controls the smoothness of the transition. We used $l_{tr} = \frac{2}{5}x_1$ in

our calculations corresponding to a relatively sharp transition. Larger values of l_{tr} would effectively mean that the leads n dope the N region of the junction and the doping there would therefore not be determined by U_p.

Finally, superconductivity in the S terminals is modelled by a on-site, complex pair-potential Δ which goes to zero as a step-function at the S-N interface. We made sure that the Fermi-wavelengths λ_N and λ_S in the N and S regions, respectively, satisfy $\lambda_S \ll \lambda_N$. This ensures that the exact spatial dependence of the superconducting pair potential at the N-S interface is not very important in the calculations.[10]

Density dependence of the critical current

Our numerical calculation for I_c as a function of doping, assuming a backgate dependent charge density profile (as described above), is shown in Figure S13. Comparing our calculations to the measurement results shown in the inset of Figure 3(a) of the main text, one can see that the I_c vs doping dependence is qualitatively very similar. In particular, the the asymmetry between the n and p doped regimes is clearly present in the calculations.

Regarding the absolute values of I_c, for $n = 2 \times 10^{11}/\mathrm{cm}^2$ we find $I_c = 7.4\mu\mathrm{A}$. The difference with respect to the prediction of Reference[10] is mainly due to the fact that in our case $L \lesssim \xi_0$. This has twofold effect: First, the contribution of the continuum states cannot be neglected. Second, the contribution of the ABSs to the supercurrent itself depends on the L/ξ_0 ratio and in our case it is smaller than what one would obtain in the strict short junction limit. Looking now at the experimental results (inset of Fig. 3a in main text), for $n = 2 \times 10^{11}/\mathrm{cm}^2$ we have measured $I_{c,exp} \approx 3\mu A$, which is less than half of what our calculations give. The reason for this discrepancy is not clear at the moment. As mentioned below, assuming a soft superconducting gap can noticeably affect the value of the calculated critical current I_c, especially for high n doping. However, for reasonable values of η we still obtain twice as large I_c as in the measurements. We note that a similar discrepancy was noted in Ref.[8] as well. They used the formula $I_c = \alpha\Delta/eR_n$, where theoretical calculations

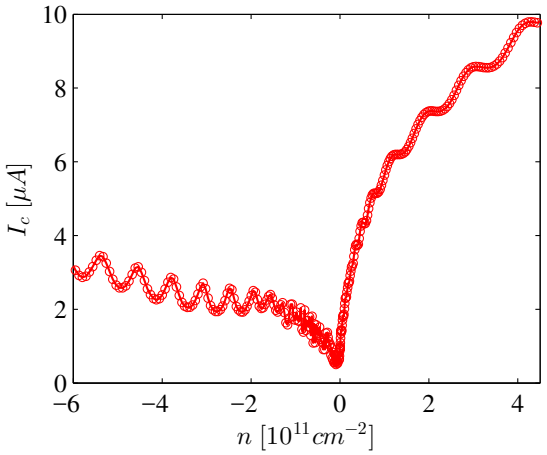

Figure S13: Theoretical calculation of the critical current I_c vs doping. The width of the junction is $W = 2\mu$m and $L/\xi_0 = 0.73$.

give a value $\alpha \approx 2.1 - 2.44$.[10] The measurement of Ref.[8] found $\alpha \approx 0.4$, i.e., a factor of $\approx 5 - 6$ difference. This is roughly the same, as the difference between the prediction of Ref.[10] and our measurements.

Soft vs hard superconducting gap

Following Reference,[11] we also considered the effect of quasiparticle broadening in the superconducting terminals by introducing a complex energy shift $E \to E + i\eta$ in the self-energy calculations. Such a broadening, described by the parameter η, can arise due to scattering with phonons or other electrons or due to other effects leading to quasiparticle poisoning.

We find that a finite η can considerably affect the value of the calculated critical current I_c. Since I_c is not the main focus of this work, we do not discuss the details here. Instead, we present results to illustrate the effect of η on the skewness. We repeated the calculations using $\eta = 0.17\Delta$ and the results are shown in Figure S14. Comparing Figure 4(c) in the main text and Figure S14, one can notice that the results are qualitatively very similar, but for $\eta = 0$ the average skewness is larger for both npn and $nn'n$ doping than for $\eta \neq 0$. We note that in the $nn'n$ regime the calculated average skewness $\bar{S} = 0.27$ for $\eta = 0$ is closer to the measured one $S_{exp} \approx 0.28$ than the result $\bar{S} = 0.22$ for $\eta = 0.17\Delta$. The opposite is true in

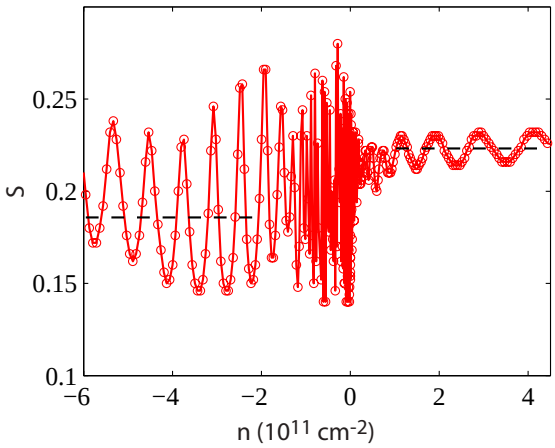

Figure S14: The calculated skewness vs doping for soft superconducting gap, i.e., $\eta = 0.17\Delta$.

the *npn* regime, where the calculations with $\eta = 0.17\Delta$ ($\eta = 0$) yielding $\bar{S} = 0.19$ ($\bar{S} = 0.22$) give better agreement with the measurements ($S_{exp} \approx 0.2$). We were not able to achieve an equally good agreement in both the *npn* and $nn'n$ regimes using a single value of η. This may indicate that η depends on the doping of the junction, but one would need a more microscopic understanding of the processes that contribute to η.

We emphasize, however, that η is not the only parameter which can affect the value of the skewness. Generally, the value of the skewness depends on the interface between the S and N regions. Calculations not shown here indicated that the presence/absence of a smooth transition between the highly doped leads and the normal graphene region (the parameter l_{tr} in Eq.12) and the value of the hopping amplitude γ_{sc} in Figure S11(b) between the S and N regions can also affect the results. However, we fixed the value of the parameters describing the junction such that we obtain a qualitatively good agreement for R_n (as discussed previously) and did not changed these parameters in the skewness calculations.

Calculations using the side contact geometry

We also performed calculations using the side-contact geometry, which is shown in Figure S11(b). This contact geometry has recently been employed, e.g., in Reference[12] to model diffusive graphene JJs both in the short and in the long junction regime. The most

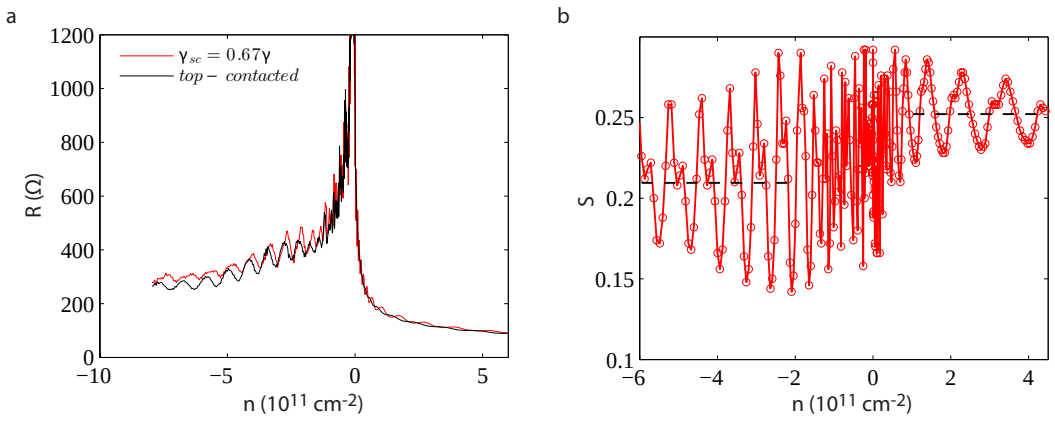

Figure S15: (a) Comparison of the calculated normal state resistance vs doping for top- and side-contacted junctions, (b) Skewness vs doping calculated in the side-contact geometry. Dashed lines indicate the average skewness in the n and p doped regime.

important results of our calculations are shown in Figure S15. We have used the same doping profile $U(x)$ along the junction as in the top-contact geometry. As it can be seen in Figure S15(a), by choosing $\gamma_{sc} = 0.67\gamma$, the doping dependence of the normal state resistance is qualitatively very similar for both models. One can notice, however, that the amplitude of the R_n oscillations for $nn'n$ doping is larger in the side-contact geometry. In the npn regime the amplitude of the FP oscillations is somewhat different, but the oscillations are in the same phase, except for large p doping.

The skewness calculation for the side contact geometry is shown in Figure S15(b). We used the same Δ and $\eta = 0.17\Delta$ as for the corresponding calculation in the top-contact geometry. The result are qualitatively similar to those shown in Figure S14 and Figure 4(c) of the main text. In particular, the average skewness is different in the npn and $nn'n$ doping regime, but the obtained $\bar{S}$ values are larger than the ones calculated in the top-contact geometry for $\eta = 0.17\Delta$. However, the amplitude of the skewness oscillations is larger in the side-contact geometry, especially for $nn'n$ doping, where they are three times larger than in Figure 4(c) of the main text. Such large oscillations are not present in the experimental data and for this reason we find a better overall agreement between the experiments and calculations using the top-contact geometry. Finally, we briefly note in the vicinity of the

CNP one can see large oscillations in the skewness and therefore both models fail to reproduce the experimental results in this regime.

References

(1) Castellanos-Gomez, A.; Buscema, M.; Molenaar, R.; Singh, V.; Janssen, L.; van der Zant, H. S. J.; Steele, G. A. *2D Materials* **2014**, *1*, 011002.

(2) Calado, V. E.; Goswami, S.; Nanda, G.; Diez, M.; Akhmerov, A. R.; Watanabe, K.; T. Taniguchi, T. M. K.; Vandersypen, L. M. K. *Nature Nanotechnology* **2015**, *10*, 761–764.

(3) Goswami, S.; Mulazimoglu, E.; Monteiro, A. M. R. V. L.; Wölbing, R.; Koelle, D.; Kleiner, R.; Blanter, Y. M.; Vandersypen, L. M. K.; Caviglia, A. D. *Nature Nanotechnology* **2016**, *11*, 861–865.

(4) McCumber, D. E. *Journal of Applied Physics* **1968**, *39*, 3113–3118.

(5) Stewart, W. C. *Applied Physics Letters* **1968**, *12*, 277–280.

(6) Rakyta, P.; Kormányos, A.; Cserti, J. *Phys. Rev. B* **2016**, *93*, 224510.

(7) Wakabayashi, K.; Fujita, M.; Ajiki, H.; Sigrist, M. *Phys. Rev. B* **1999**, *59*, 8271–8282.

(8) Shalom, M. B.; Zhu, M. J.; Fal'ko, V. I.; Mishchenko, A.; Kretinin, A. V.; Novoselov, K. S.; Woods, C. R.; Watanabe, K.; Taniguchi, T.; Geim, A. K.; Prance, J. R. *Nature Physics* **2016**, *12*, 318.

(9) Rickhaus, P.; R. Maurand, M. H. L.; Weiss, M.; Richter, K.; Schönenberger, C. *Nature Communications* **2013**, *4*, 2342.

(10) Titov, M.; Beenakker, C. W. J. *Phys. Rev. B* **2006**, *74*, 041401.

(11) Takei, S.; Fregoso, B. M.; Hui, H. Y.; Sarma, A. M. L. S. D. *Phys. Rev. Lett.* **2013**, *110*, 186803.

(12) Li, C.; Guéron, S.; Chepelianskii, A.; Bouchiat, H. *Phys. Rev. B* **2016**, *94*, 115405.